JACS
JOURNAL OF THE AMERICAN CHEMICAL SOCIETY
pubs.acs.org/JACS
Article

Tailoring Morphology and Elemental Distribution of Cu-In Nanocrystals via Galvanic Replacement

Laia Castilla-Amorós, Pascal Schouwink,[‖] Emad Oveisi,[‖] Valery Okatenko, and Raffaella Buonsanti*

Cite This: J. Am. Chem. Soc. 2022, 144, 18286−18295

ABSTRACT: The compositional and structural diversity of bimetallic nanocrystals (NCs) provides a superior tunability of their physico-chemical properties, making them attractive for a variety of applications, including sensing and catalysis. Nevertheless, the manipulation of the properties-determining features of bimetallic NCs still remains a challenge, especially when moving away from noble metals. In this work, we explore the galvanic replacement reaction (GRR) of In NCs and a copper molecular precursor to obtain Cu-In bimetallic NCs with an unprecedented variety of morphologies and distribution of the two metals. We obtain spherical $Cu_{11}In_9$ intermetallic and patchy phase-segregated Cu-In NCs, as well as dimer-like Cu-$Cu_{11}In_9$ and Cu-In NCs. In particular, we find that segregation of the two metals occurs as the GRR progresses with time or with a higher copper precursor concentration. We discover size-dependent reaction kinetics, with the smaller In NCs undergoing a slower transition across the different Cu-In configurations. We compare the obtained results with the bulk Cu-In phase diagram and, interestingly, find that the bigger In NCs stabilize the bulk-like Cu-$Cu_{11}In_9$ configuration before their complete segregation into Cu-In NCs. Finally, we also prove the utility of the new family of Cu-In NCs as model catalysts to elucidate the impact of the metal elemental distribution on the selectivity of these bimetallics toward the electrochemical CO_2 reduction reaction. Generally, we demonstrate that the GRR is a powerful synthetic approach beyond noble metal-containing bimetallic structures, yet that the current knowledge on this reaction is challenged when oxophilic and poorly miscible metal pairs are used.

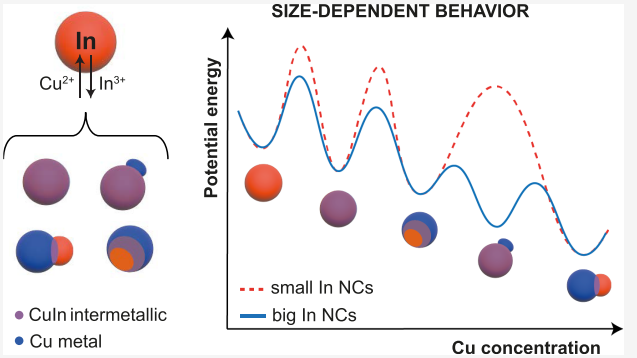

INTRODUCTION

Bimetallic nanocrystals (NCs) possess a wide tunability of their physico-chemical properties which arise from synergistic effects between the two metals altering their electronic structures.[1−15] Such tunability makes them more appealing than monometallic NCs for several applications, including sensing and catalysis.[1−15] The properties of bimetallic NCs are governed by their composition as well as by the spatial distribution of the metals within each NC (i.e., configuration); thus, learning how to control both features is of utmost importance to eventually optimize these NCs for the desired function.[16−19] First of all, the two metals can be either alloyed or phase-segregated. Alloys can have both disordered and atomically ordered structures, called intermetallics.[19] When phase-segregated, many configurations are possible, including core@shell NCs and dimer-like NCs.[20]

The miscibility between the two metals is one of the main forces regulating the extent of mixing.[21] Generally, this principle applies to both bulk and nanomaterials. Yet, how immiscible metals distribute within nanoscale objects and how to eventually control their distribution remain poorly understood.[22,23] Furthermore, alloys of immiscible metals can be obtained at the nanoscale, especially when kinetically controlled synthetic approaches are employed.[20] Miscibility can also change at the nanoscale and exhibit size dependence.[23−25] Overall, to advance the current state of the art in the synthesis of this important class of nanomaterials, increasing efforts should be directed toward understanding how to controllably target bimetallic NCs with tunable composition and configuration.

Colloidal synthesis is a powerful and versatile approach to form bimetallic NCs with tunable sizes, shapes, compositions, and crystal structures.[1,7,19,26−28] The control over several reaction parameters has proven useful to advance the mechanistic knowledge on the factors determining the composition and configuration of multicomponent NCs.[22,29−31] As for metals, most studies have been performed on noble metal-containing NCs, for which a vast library of

Received: June 1, 2022
Published: September 29, 2022

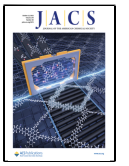

https://doi.org/10.1021/jacs.2c05792
J. Am. Chem. Soc. 2022, 144, 18286−18295

bimetallic structures exists.[7] The oxophilicity of other metals complicates their synthesis and makes working with them more unpredictable.[32] For example, the presence of a native oxide surface around Ga or Mn results in phase-segregated dimeric structures following galvanic replacement, instead of the alloys and hollow structures which were expected based on the existing knowledge on noble metal NCs.[27,33] Yet, non-noble metals are certainly not less intriguing or appealing for applications, which include plasmonics and catalysis, compared to noble metals.[33,34]

In this work, we describe the synthesis of Cu-In NCs with different configurations via a sole synthetic approach. Cu-In bimetallic NCs have recently been attracting attention particularly in the field of catalysis.[35−45] While these examples in the literature suggest the importance of composition and element distribution as properties-determining features,[31−41] a suitable synthesis allowing for monodispersed and tunable NCs that could serve as a study platform to exploit the potential of these bimetallic particles remains to be found. We use In NCs as sacrificial seeds for a galvanic replacement reaction (GRR) with a copper molecular precursor and obtain intermetallic and phase-segregated Cu-In NCs by simply tuning the reaction time and/or the precursors' ratio. Structural and compositional characterization of different samples reveals size-dependent kinetics in a reaction process involving first alloying, to form $Cu_{11}In_9$ intermetallic NCs, followed by dealloying into Cu-In dimers, for which arguments are provided. We also isolate bulk-like Cu-$Cu_{11}In_9$ NCs when using bigger In NC templates; these Cu-$Cu_{11}In_9$ NCs are not accessible in smaller NCs, which we attribute to size-dependent strain effects. We demonstrate that nontypical GRR outcomes, "typical" indicating the formation of alloyed and hollow particles obtained from noble metals, can be expected for more oxophilic metal pairs.

EXPERIMENTAL SECTION

Materials and Chemicals. Copper(II) acetate ($Cu(OAc)_2$, 99.999%), oleic acid ($C_{17}H_{33}CO_2H$ or OLAC, 90%), 1-octadecene ($C_{18}H_{36}$ or ODE, 90%), and oleylamine ($C_{18}H_{35}NH_2$ or OLAM, 70% and 80−90%) were all purchased from Sigma-Aldrich. ODE, OLAC, and OLAM were degassed and dried under vacuum at 110 °C for 4 h, cooled down to room temperature, and then transferred airless to the glovebox in sealed vials. All syntheses were carried out under an inert atmosphere using anhydrous solvents and standard glovebox and Schlenk-line techniques. Postsynthetic purification ("washing"), handling and storage of the as-synthesized materials were also carried out under an inert atmosphere.

Synthesis. *Cu-In NCs.* In NCs were synthesized by adapting a literature procedure[26] (details in the Supporting Information). In a typical synthesis of Cu-In NCs, 1 mL of 4 mM solution of In NCs in ODE, 1.5 mL of a 4 mM solution of $Cu(OAc)_2$ in ODE (0.006 mmol), 0.5 mL of OLAC, and 0.5 mL of OLAM were added to a 5 mL vial. The vial was then stirred on a hot plate which was set at 160 °C (a thermocouple positioned inside the reaction medium indicates a temperature of around 128 °C), inside a glovebox for variable time from 15 to 120 min, depending on the desired structures. The reaction product was separated from byproducts and from unreacted precursors by adding anhydrous ethanol (3 mL), followed by centrifugation at 6000 rpm for 10 min. Cu-In NCs were redispersed in anhydrous toluene, and the purification/precipitation step was repeated 2−3 times before finally being stored in anhydrous toluene. As described in the Results and Discussion section of this text, as well as in the Supporting Information, the size, morphology, and elemental composition and distribution of Cu-In NCs were tuned by adjusting the size of the In NCs, the reaction time, and the volume of the added $Cu(OAc)_2$ solution.

Characterization. *Electron Microscopy.* Transmission electron microscopy (TEM) images were recorded on a Thermo Fisher Scientific Tecnai-Spirit at 120 kV, equipped with a Gatan camera. High-angle annular dark-field scanning TEM (HAADF-STEM) imaging and energy-dispersive X-ray spectroscopy (EDXS) were performed on a Thermo Fisher Scientific Tecnai-Osiris TEM in a scanning mode at an accelerating voltage of 200 kV. Atomic HAADF-STEM images were acquired on a double Cs-corrected Thermo Fisher Scientific Titan Themis 60−300 operated at 200 kV. Both Tecnai-Osiris and Titan Themis microscopes are equipped with a high brightness Schottky X-FEG gun, four silicon drift Super-X EDXS detectors, and Bruker and Velox acquisition software. EDXS data were collected in the form of spectrum images, in which a focused electron probe was scanned in a raster across a region of interest in the scanning TEM (STEM) mode. Samples were drop-cast on either a copper or gold TEM grid (Ted Pella, Inc.) prior to imaging.

Inductively Coupled Plasma-Optical Emission Spectroscopy. Previously dried samples were digested with concentrated HNO_3 and then diluted for analysis. The concentrations of the NP solutions were determined on an Agilent 5110 inductively coupled plasma-optical emission spectrometry (ICP-OES) system with a VistaChip II CCD detector.

Grazing-Incidence X-ray Diffraction. Grazing-incidence X-ray diffraction (GI-XRD) was performed at a 0.5° incidence angle on a Bruker D8 Discover Plus equipped with a Cu-rotating anode and a Dectris Eiger2 detector. GID data were refined with Topas using the Rietveld method, heavily constraining displacement parameters and peak shapes due to the limited data quality. Preferred orientation corrections had to be included for certain phases. Samples were prepared by drop-casting the NC solution on silicon substrates that had previously been washed with isopropanol and acetone.

Electrocatalytic Measurements. *Electrode Preparation.* Glassy carbon plates (2.5 × 2.5 cm^2, Sigradur G, HTW) coated with the NCs were used as the working electrode. 15 μg of each sample dispersed in 14 μL of toluene was drop-cast onto a circular area of 1.33 cm^2 on the glassy carbon plates. After drop-casting, the electrodes were rinsed with ethanol and water, blown dry with N_2, and tested.

Electrochemical Measurements. All the electrochemical measurements were performed with a Biologic SP-300 potentiostat and carried out in a gas-tight electrochemical H-cell built in our laboratory. The catholyte and anolyte compartments are separated by a Selemion AMV anion exchange membrane and were filled with 2 mL of electrolyte each to concentrate and allow liquid product detection. Pt foil was used as the counter electrode, and Ag/AgCl electrode (leak free series) (Innovative Instruments, Inc.) was used as the reference electrode.

A CO_2-saturated 0.1 M $KHCO_3$ solution was used as an electrolyte. To prepare such a solution, 0.276 g of K_2CO_3 was diluted in 40 mL of Milli-Q water to obtain a 0.05 M K_2CO_3 solution, which was bubbled for 30 min with CO_2 (99.999%, Carbagas) prior to the start of measurements. During electrolysis, CO_2 was prehumidified by passing its flow through a water bubbler and constantly supplied to both cell compartments via ceramic frits at a flow rate of 5 sccm each. With this, the gas was bubbled through the electrolyte to prevent CO_2 depletion, as well as to allow continuous analysis of gaseous products via a gas chromatograph. A mass flow controller (Bronkhorst) was used to control the flow rate of CO_2. The experiments were performed in a chronoamperometry mode.

Electrochemical impedance spectroscopy (EIS) was performed prior to the main measurement to determine the electrochemical cell resistance (R_{cell}) and compensate for the ohmic losses. Four spectra were measured at the open-circuit potential, using 41 points between 1 MHz and 100 Hz, using a sinus amplitude of 20 mV and a pause time of 0.6 s between each frequency. Software utility in-built into the potentiostat software (EC-lab) was used to apply the ohmic loss correction to further measurement.

Product Analysis. A gas chromatograph (GC, SRI instruments) equipped with a HayeSep D porous polymer column, a thermal conductivity detector, and a flame ionization detector was used for the analysis of gaseous products. GC was calibrated for H_2, CO, CH_4,

https://doi.org/10.1021/jacs.2c05792
J. Am. Chem. Soc. 2022, 144, 18286−18295

C_2H_4, and C_2H_6. Five standard gas mixtures (Carbagas) were used to obtain the calibration plots for the determination of gaseous product concentrations. Ultra-high-purity N_2 (99.999%) was used as a carrier gas.

The Faradaic efficiency (FE) for the gaseous products is calculated with the following equation:

$$\mathrm{FE} = \frac{n_e \times F \times C \times f \times P}{R \times T \times I}$$

where n_e is the number of electrons transferred to product formation; F is the Faraday constant (96,485 C mol^{-1}); C is the measured concentration of the product by GC (in ppm); f is the gas flow rate (mL s^{-1}); P is the pressure (1.01×10^5 Pa); I is the imposed current (in A); R is the universal gas constant (8.314 J mol^{-1} K^{-1}), and T is the temperature (K). Values obtained after 10 min of electrolysis are not included in the calculation of FE as GC gas flow is not yet stabilized at that point.

The FE of liquid products was determined in a similar manner. 0.4 mL of both the catholyte and the anolyte was collected and analyzed with high-performance liquid chromatography (HPLC) on the UltiMate 3000 instrument from Thermo Scientific, which is equipped with a refractive index detector for product quantification and an Aminex HPX-87H (BioRad) column for product separation (1 mM H_2SO_4 was used as an eluent). The necessity to collect the electrolyte from both compartments is reasoned by the possible product crossover from the catholyte to the anolyte compartment.

The resulting formula used for calculations of liquid products FE is

$$\mathrm{FE} = \frac{n_e \times F \times C}{V \times I \times t}$$

where n_e is the number of electrons transferred to product formation; F is the Faraday constant; C is the measured concentration of the product by HPLC (mol mL^{-1}); V is the cell volume (4 mL); I is the measured current (A); and t is the duration of electrolysis (2700 s).

The electrode potential is recalculated with respect to the RHE reference using iR compensation according to the equation:

$$E_{\mathrm{RHE}} = E_{\mathrm{Ref}} + 0.206 + 0.0591 \times \mathrm{pH} - (R_{\mathrm{cell}} \times I)$$

where E_{Ref} is the recorded potential against the Ag/AgCl reference electrode (V); +0.206 V is the Ag/AgCl reference electrode correction; R_{cell} is the ohmic resistance between the working and the reference electrode, which was defined using EIS analysis prior to the measurement (Ohm); and I is the imposed current (A).

All the experiments in this work were run for 45 min, and the FE and current density averaged over this time.

RESULTS AND DISCUSSION

Monodisperse colloidal In NCs of 15 nm were synthesized by adapting a previously reported procedure (Figure S1).[26] By modifying an earlier synthesis protocol developed for Cu-Ga nanodimers,[27] In NCs were reacted with a copper molecular precursor at 160 °C for 30, 60, and 120 min. The copper molecular precursor is a copper(II)-oleylamine complex forming in the reaction mixture.[27] GRRs are electrochemical processes in which a sacrificial metal (herein metallic In, $E^{\circ}_{In^{3+}/In^0} = -0.34$ V) is oxidized by a metal cation in solution possessing a more positive redox potential (herein Cu^{2+}, $E^{\circ}_{Cu^{2+}/Cu^0} = 0.34$ V) that, in turn, gets reduced and deposits onto the preexisting template.[27,46−52]

First, the GRR outcome was characterized as a function of time while keeping the Cu:In ratio constant; Cu-In bimetallic NCs with different morphologies and elemental distribution were isolated (Figure 1a). TEM characterization provides an overview of the bimetallic NC morphology (Figure 1b−d). At 30 and 60 min, spherical NCs are observed, with no visible changes in morphology and similar size distribution compared

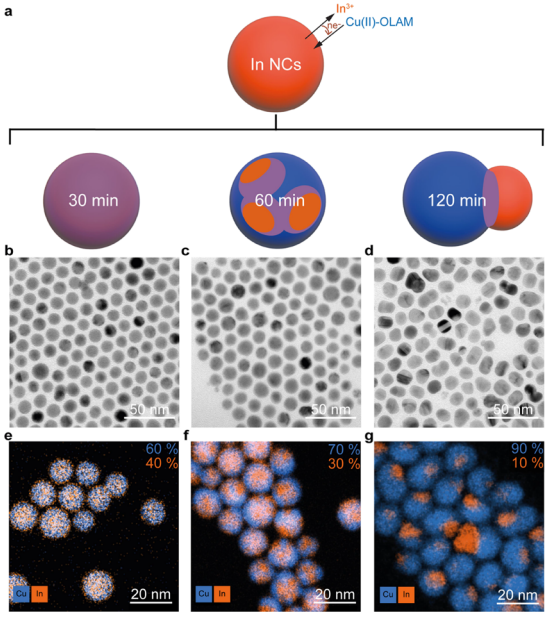

Figure 1. (a) Schematic representation of the reaction scheme and of the resulting products depending on the reaction time; (b−d) bright-field TEM images and (e−g) STEM-EDXS elemental maps of Cu and In of the as-synthesized Cu-In NCs obtained at 30 min (b,e), 60 min (c,f), and 120 min (d,g). The Cu and In contents measured by EDXS quantification are reported on the top right of EDXS maps (e−g); they indicate an increase in Cu content with reaction time. For all samples, 15 nm In NCs were used as sacrificial GRR seeds, and the precursor ratio was set at 0.004 mmol of In and 0.006 mmol of Cu (see Supporting Information and Tables S1 and S2 for additional details).

to the parental In NCs (Figures 1b,c and S1 and Table S2). Instead, at 120 min, the NCs turn into elongated dimer-like structures (Figure 1d). STEM-EDXS elemental maps show that the element distribution changes over time within the NCs while remaining uniform within each sample (Figure 1e−g). The spherical NCs obtained at 30 min possess a homogeneous distribution of Cu and In (Figure 1e). At longer reaction times, the two elements segregate. Segregation is already noticeable in the sample obtained at 60 min (Figure 1f); after 120 min, Cu and In exist as completely separated domains sharing an interface within the dimer-like NCs (Figure 1g). Quantitative elemental analysis of these samples by EDXS and ICP-OES evidenced that more Cu is incorporated in the NCs as the reaction time increases, which is consistent with the GRR mechanism. Specifically, the average atomic Cu content measured with both EDXS over a larger region of particles and elemental ICP analysis was 60, 70, and 90% (at.%) for the NC samples obtained at 30, 60, and 120 min of reaction time, respectively. Notably, a sharp transition from 1 to 60 at.% Cu content, with no intermediate compositions, was observed with either shorter reaction times or lower amounts of the Cu precursor (Figure S2 and Table S3).

Atomic resolution HAADF-STEM and corresponding STEM-EDXS elemental maps of individual particles (Figures 2a−f and S4) combined with GI-XRD (Figures 2g and S3) provide additional compositional and structural details. After 30 min of reaction, Cu-In NCs possess a homogeneous crystalline core, with interatomic distances corresponding to the $Cu_{11}In_9$ intermetallic phase, which are identified by

https://doi.org/10.1021/jacs.2c05792
J. Am. Chem. Soc. 2022, 144, 18286−18295

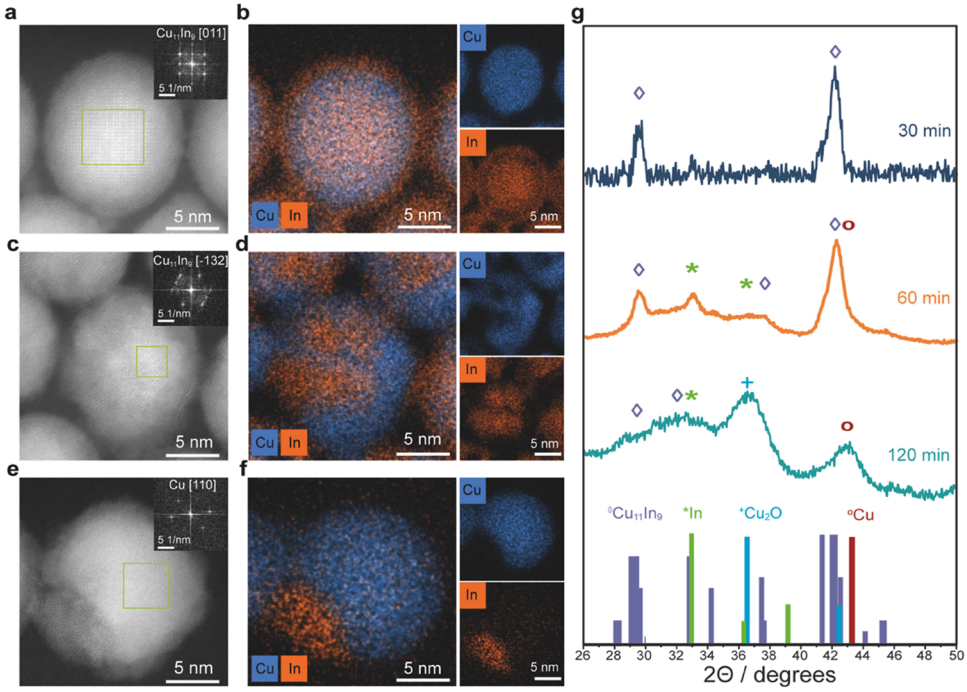

Figure 2. Atomic resolution HAADF-STEM images, including FFT of the selected areas in green, with their corresponding STEM-EDXS elemental mapping of individual as-synthesized Cu-In NCs after (a,b) 30 min, (c,d) 60 min, and (e,f) 120 min of reaction time. Oxygen STEM-EDXS elemental mapping of these images can be found in Figure S4; (g) GI-XRD patterns of the Cu-In NCs obtained at different reaction times as indicated by the labels. At the bottom, standard patterns of In (PDF 00-005-0642), $Cu_{11}In_9$ (PDF 00-041-0883), Cu (PDF 00-004-0836), and Cu_2O (PDF 01-078-2076).

analyzing the resulting FFT of the atomic resolution HAADF-STEM image, surrounded by an amorphous indium oxide shell (Figure 2a,b). The corresponding GI-XRD pattern is consistent with $Cu_{11}In_9$ being the major crystalline component in the sample (Figures 2g and S3). The elemental quantification of 60 at.% Cu and 40 at.% In is also close to the $Cu_{11}In_9$ elemental ratio (55 at.% Cu, 45 at.% In). After 60 min, the patchy spatial segregation of In and Cu elements is accompanied by the progressive transformation of $Cu_{11}In_9$ into other nanocrystalline phases, which generates more heterogeneities within the particle (Figure 2c). The corresponding GI-XRD pattern of these NCs could be refined for In, Cu (both as Cu and Cu_2O), and $Cu_{11}In_9$ intermetallic (Figures 2g and S3). Finally, in the dimer-like Cu-In NCs obtained after 120 min of reaction, only the Cu domains could be aligned along a major zone axis and confirmed to be metallic Cu from the FFT analysis of the corresponding HAADF-STEM image (Figure 2e). Concomitantly, the GI-XRD pattern indicates Cu and Cu_2O as the major crystalline components, which is in agreement with the elemental analysis indicating 90 at.% of Cu. Metallic In and the $Cu_{11}In_9$ intermetallic are also identified as two minor phases in the GI-XRD pattern. As the FFT indicates purely metallic Cu and TEM measurements are performed in vacuum, the Cu_2O detected in the XRD patterns most likely derives from oxidation during sample manipulation and data acquisition. The coupling of the XRD result with the EDXS mapping suggests that the dimer-like NCs obtained after 120 min of reaction consist of one domain of Cu/Cu_2O and one domain of In and $Cu_{11}In_9$, probably as a shared interface.

Altogether, a first mechanistic picture of the GRR between In NCs and the Cu precursor starts to shape up. In the initial stages of the reaction, Cu incorporates into the In NCs and forms the intermetallic $Cu_{11}In_9$ structure without any intermediate alloy structures. This behavior is consistent with the bulk phase diagram (Figure S5).[53] As the GRR proceeds, more In is replaced by Cu. When the Cu content increases over 60 at. %, dealloying and phase segregation into Cu, In, and $Cu_{11}In_9$ takes place toward the final dimer-like Cu-In NCs. Interestingly, the Cu-In bulk phase diagram indicates that, at temperatures below 160 °C, which is the reaction temperature, Cu and $Cu_{11}In_9$ intermetallic should coexist, without segregation of In, for compositions containing more than 60% Cu (Figure S5).[53] Differences between the bulk phase diagram and the behavior observed at the nanoscale are not uncommon. For example, alloying and dealloying phenomena leading to the coexistence of Cu, Cu-In, and In have been observed in thin films.[54−56] Stabilization of phases different from those reported for bulk materials can occur in thin films and in NCs as a result of thermodynamics (i.e., increased significance of the surface free energy term as the thickness or size decreases) or kinetics (i.e., reaction proceeding under out-of-equilibrium conditions).[57,58] Dealloying of bimetallic NCs, those including metals of different oxophilicities, has indeed been reported under nonequilibrium conditions and during GRRs.[46,59−65] To understand the role of size in the phase segregation and deviation from the bulk phase diagram in the Cu-In NCs, we performed GRRs between larger In NCs of 19 and 22 nm and the Cu precursor under the same reaction conditions.

19 and 22 nm In NCs were synthesized by modifying the reaction time of the same procedure followed for the 15 nm In NCs (Figure S6). Hereafter, Cu-In NCs will be labeled as Cu-In15, Cu-In19, and Cu-In22 depending on the size of the In NC seeds, being 15, 19, and 22 nm, respectively. Cu-In19/22 NCs with different composition, elemental distribution, and morphology were synthesized by tuning the amount of the

https://doi.org/10.1021/jacs.2c05792
J. Am. Chem. Soc. 2022, 144, 18286−18295

copper precursor added and/or the reaction time, as done for the Cu-In15 NCs discussed so far. The complete set of experiments is reported in Figure S7 with details in Table S4. Figure 3 reports data on the most relevant and representative samples.

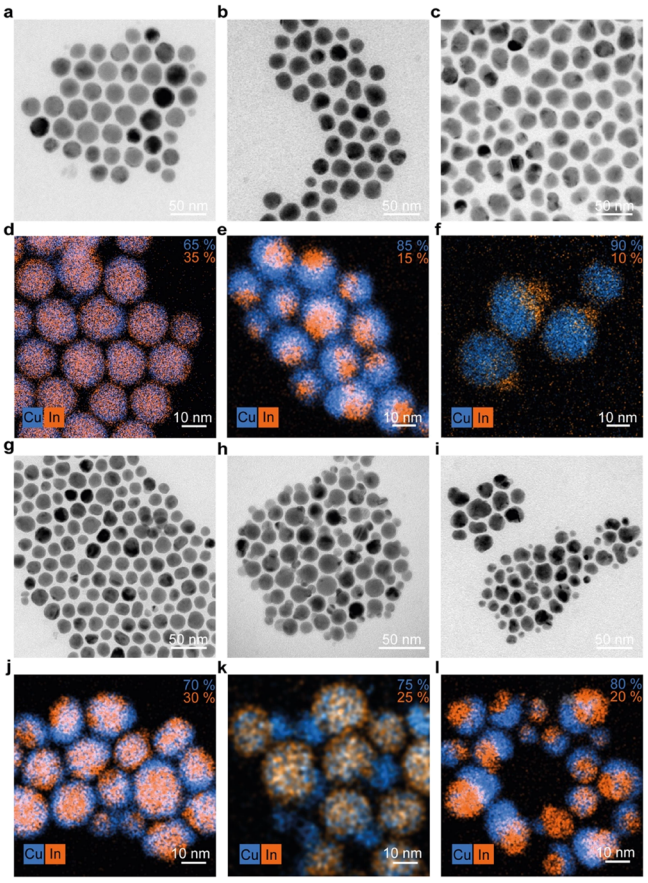

Figure 3. (a–c) Bright-field TEM images and (d–f) STEM-EDXS elemental maps of Cu-In19 NCs with increasing Cu content; these samples were synthesized by fixing the reaction time at 30 min and increasing the added Cu molecular precursor (0.0015, 0.003, and 0.006 mmol, respectively) for the same amount of In (0.004 mmol) (Table S4). 19 nm In NCs were used as sacrificial GRR seeds. (g–i) Bright-field TEM images and (j–l) STEM-EDXS elemental maps of Cu-In22 NCs with increasing Cu content; these samples were synthesized by fixing the reaction time at 30 min and increasing the added Cu molecular precursor (0.0015 mmol for g,j and 0.006 mmol for h,k) or increasing the reaction time (0.006 mmol of Cu and 60 min for i,l) for the same amount of In (0.004 mmol) (Table S4). 22 nm In NCs were used as sacrificial GRR seeds. For all samples, the Cu and In contents measured by EDXS quantification are reported on the top right of the EDXS maps.

In the case of the Cu-In19 NCs, the three previously discussed GRR stages, which are homogeneously mixed (Figure 3a,d), patchy phase-segregated (Figure 3b,e), and dimer-like (Figure 3c,f) NCs were obtained by tuning the added amount of the Cu precursor for a reaction time of 30 min. Notably, the formation of dimer-like Cu-In15 NCs required longer times (i.e., 120 min) with the highest amount of the Cu precursor (i.e., 0.006 mmol), which indicates faster reaction kinetics with these bigger In NCs.

A different picture arises for the Cu-In22 NCs (Figure 3g–l). First, the Cu-In22 NCs become slightly elongated already after 30 min with the lowest amount of the Cu precursor (i.e., 0.0015 mmol) (Figure 3g). STEM-EDXS elemental maps indicate the presence of a pure Cu domain around an area with uniformly mixed Cu and In (Figure 3j). The addition of more Cu generates well-defined dimer-like NCs (Figure 3h). These dimers consist of one domain of Cu interfaced with a larger domain where Cu and In are homogeneously mixed (Figure 3k). Only increasing the reaction time eventually forms the dimer-like NCs where Cu and In are separated into two distinct domains, equivalent to those observed for Cu-In15/19 NCs (Figure 3i,l).

The newly obtained dimer-like Cu-In22 intermediates were characterized in more detail (Figures 4 and S8). The GI-XRD pattern perfectly matched the $Cu_{11}In_9$ intermetallic phase (Figure 4a), with the Cu domain being probably too small and overlapped with the intermetallic signal to be deconvoluted. The corresponding atomic resolution HAADF-STEM image, including the FFT of the selected area in green (Figure 4b), and STEM-EDXS elemental mapping (Figure 4c) performed at a single particle level are consistent with the bigger domain being the intermetallic phase and the smaller domain being copper.

Altogether, the expansion of the GRR to bigger In NC seeds enables the construction of a full mechanistic picture of the Cu-In NC formation, which is summarized in Figure 5. Starting with metallic In NCs, Cu incorporates into the particle to form $Cu_{11}In_9$ intermetallic NCs. In agreement with the bulk thermodynamics of the system, no other alloys are isolated before the formation of the intermetallic phase. Additional incorporation of Cu results into their transition to phase-segregated dimer-like Cu-In NCs. The intermediate structures are patchy phase-segregated spherical NCs including Cu, In, and $Cu_{11}In_9$ domains for smaller-sized In NCs, while dimer-like Cu-$Cu_{11}In_9$ NCs are identified for bigger In NCs. This Cu-$Cu_{11}In_9$ biphasic configuration is more consistent with the Cu-In bulk thermodynamics as discussed in previous paragraphs.

The results indicate that size effects impact the GRR outcome and, more generally, the behavior of the Cu-In system at the nanoscale. First, the GRR proceeds faster for bigger NCs than for smaller NCs. Second, the larger NCs do enable us to capture structures which more closely resemble the composition expected by the bulk phase diagram.

To the best of our knowledge, no previous studies have investigated the sole size dependence of the GRR as size effects have often been convoluted with surface facet effects.[66]

The driving force for GRR is the difference in the redox potentials of In and Cu. Considering the size range of the In NCs, it is reasonable to assume that their initial redox properties are equivalent.[67] The shorter diffusion length of smaller particles should promote faster alloying/dealloying, which is not the case for the system discussed in this work.

Only a handful of studies have specifically tackled the size dependence of alloying and dealloying in NCs.[63,68] Gezelter and co-workers found that Au–Ag alloying is faster in smaller particles,[68] which one could attribute to shorter diffusion lengths. However, as Au and Ag are miscible metals over a wide compositional range, the same principles are not applicable to Cu-In.

Keeping in mind the immiscibility over a wide compositional range and the different crystalline structures of the two metals and the intermetallic phase (In is tetragonal with $a = b = 3.252$ Å, $c = 4.946$ Å, $\beta = 90°$; Cu is fcc with $a = b = c = 3.615$ Å, $\beta = 90°$ and $Cu_{11}In_9$ is monoclinic with $a = 12.821$ Å, $b = 4.355$ Å,

https://doi.org/10.1021/jacs.2c05792
J. Am. Chem. Soc. 2022, 144, 18286–18295

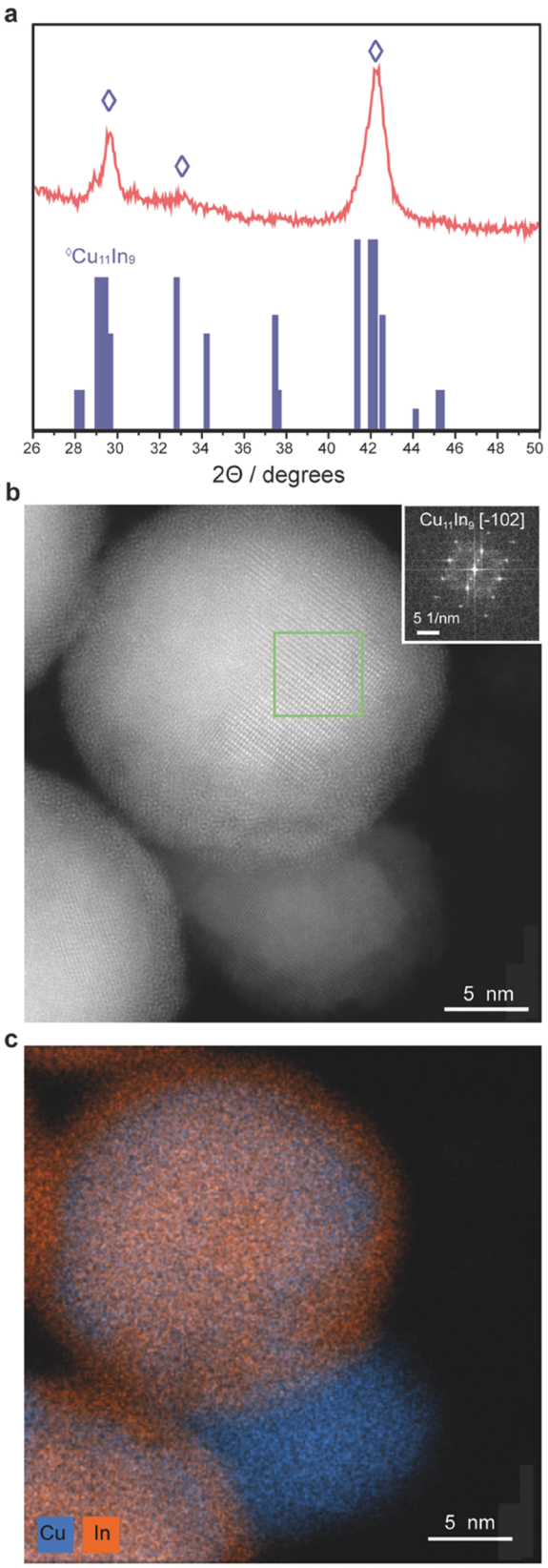

Figure 4. (a) GI-XRD pattern of the dimer-like Cu-In22 NCs at the bottom standard pattern of $Cu_{11}In_9$ (PDF 00-041-0883); (b) atomic resolution HAADF-STEM of an individual dimer, including the FFT of the selected area in green corresponding to the $Cu_{11}In_9$ intermetallic; and (c) STEM-EDXS elemental mapping of the same particle.

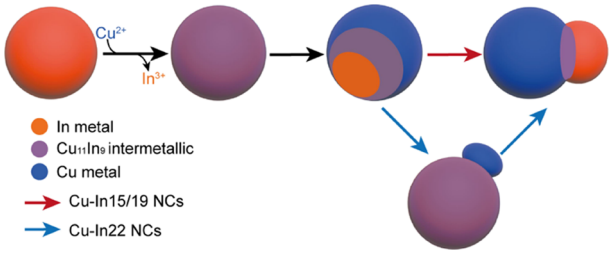

Figure 5. Schematic illustration of the reaction between In NCs and the copper precursor to form different Cu-In NCs as the reaction time is extended or the amount of the copper precursor is increased. Independently of the In size, intermetallic spheres and Cu-($Cu_{11}In_9$)-In nanodimers are obtained. Different pathways are shown for the Cu-In15/19 NCs (red arrow) and the Cu-In22 NCs with their intermediate step (blue arrow).

c = 7.357 Å, β = 125.523°), the initial replacement of In by Cu atoms will most likely induce strain into the In NCs. The smaller the NCs are, the more strained their structure will be due to the increased number of surface and interface atoms,[69] which will also hinder the transition toward the intermetallic stable phase. This phenomenon can reasonably explain the slower reaction kinetics of the smaller In NCs in the GRR with Cu to form the $Cu_{11}In_9$ intermetallic.

As the GRR proceeds, the larger particles also undergo a faster dealloying process. This observation is consistent with the results from Strasser and co-workers on Pt−Co and Pt−Cu, although the authors do not provide a fundamental reason for their result.[63] As mentioned earlier, the bigger NCs do enable us to capture a different intermediate, which is the Cu-$Cu_{11}In_9$ biphasic configuration. One possible explanation to the observation of this structure only for the bigger In NCs can be found in the strain exerted on the chemical bonds in the vicinity of the Cu/$Cu_{11}In_9$ interface. The atomic structures of the very simple fcc-Cu and the rather complex $Cu_{11}In_9$ intermetallic do not allow for an obvious epitaxial relationship in the conventional picture of lattice mismatch.[70] Indeed, only fragments of the fcc-Cu structure match the monoclinic $Cu_{11}In_9$ intermetallic, with average Cu−Cu distances approx. 6% larger in the latter (Figure S9). Smaller particle sizes might increase further this bond distance mismatch, thus making it prohibitive for a Cu/$Cu_{11}In_9$ interface to exist. This effect might explain why the Cu-$Cu_{11}In_9$ dimeric structures are observed only for the bigger In NCs. It is worth noting that the situation may be much more complex, with an interface including locally intertwined domains or amorphous volume fractions. These questions cannot be answered based on the current imaging as the interface is not stable and reconstruct under the electron beam while tilting the sample. Nevertheless, the existence of the Cu-$Cu_{11}In_9$ dimeric structure represents an additional local minimum in the free energy diagram of the bigger NCs and might be responsible for reducing the kinetic barrier needed for dealloying, thus facilitating the formation of the final dimer-like Cu-In NCs sharing a $Cu_{11}In_9$ interphase. The phase segregation of indium is not contemplated by the bulk phase diagram. However, these NCs form under out-of-equilibrium conditions, where an electrochemical potential drives the substitution of In in $Cu_{11}In_9$ with Cu, which might explain such deviation from the ideal behavior expected under purely thermodynamic conditions.

Following the idea of representing colloidal synthesis as trajectories on the potential energy surface leading to various

https://doi.org/10.1021/jacs.2c05792
J. Am. Chem. Soc. 2022, 144, 18286−18295

reaction products,[71] the energy landscape of the Cu-In NC synthesis can be drawn as a function of the Cu concentration (Figure 6). While the full energy landscape can be complicated,

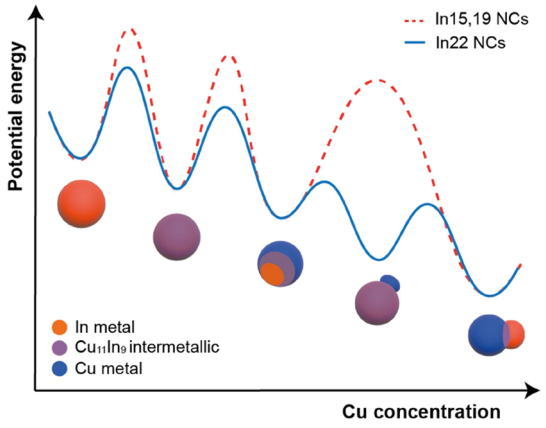

Figure 6. Potential energy landscape for the formation of Cu-In NCs starting from In NCs via GRR for different Cu concentrations. The slower alloying and dealloying kinetics of the 15 and 19 nm In NCs compared to that of the 22 In NCs are attributed to the higher energy barriers imposed by the structural strain induced by the Cu incorporation into the In structure. Because of their capacity to easy strain release, the bigger In NC seeds stabilize the more bulk-like Cu-$Cu_{11}In_9$ structure, which facilitates their conversion into the most thermodynamically stable dimer-like Cu-In NCs.

for example, by additional minima and activation barriers associated with ligand desorption and reorganization, and keeping in mind that the relative potential energy of the different configuration is qualitative, the simplified schematics still serves its purpose. It is noted that higher reaction temperatures do increase the reaction kinetics (Figure S10); however, the In NCs convert from solid to liquid at temperature above 160 °C,[72] thus the results are not comparable with those described above. The reaction does not proceed at lower temperatures (Figure S11), with one possible reason being that the energy provided to the system is insufficient for the formation of the intermetallic phase which requires a significant structural rearrangement from tetragonal In to monoclinic $Cu_{11}In_9$, while Cu is incorporated.

Finally, we tested some of the obtained structures as catalysts for the electrochemical CO_2 reduction reaction (CO_2RR) to demonstrate their utility as the model system to elucidate structure/property relations in catalysis (Figures 7 and S12–S14). Figure 7 compares the FE of In, $Cu_{11}In_9$, Cu-In dimers, and Cu NCs tested at three different potentials (−0.6, −0.85, and −1.1 V vs RHE, reversible hydrogen electrode), which were chosen based on an initial screening performed by linear scanning voltammetry. As expected, In NCs are mostly selective for formate with a maximum $FE_{formate}$ of 45% at −0.8 V_{RHE} with a corresponding formate/CO ratio of around 4.7 (Figure S12) and a maximum formate/CO ratio of around 6.0 (Figure S12) but with a $FE_{formate}$ of around 35% at −0.6 and −1.1 V_{RHE}. Instead, Cu NCs generate beyond C1 products at cathodic enough voltages (−1.1 V_{RHE}). Interestingly, the Cu-In samples produce only formate and CO among the CO_2RR products. In particular, the $Cu_{11}In_9$ NCs maintain a preferential selectivity for formate, which is very similar to that of the pure In NCs at −0.6 V_{RHE}, with an $FE_{formate}$ of around 25% and a formate/CO ratio of 6.0 (Figure S12), with the advantage of a higher current density. Contrastingly, the

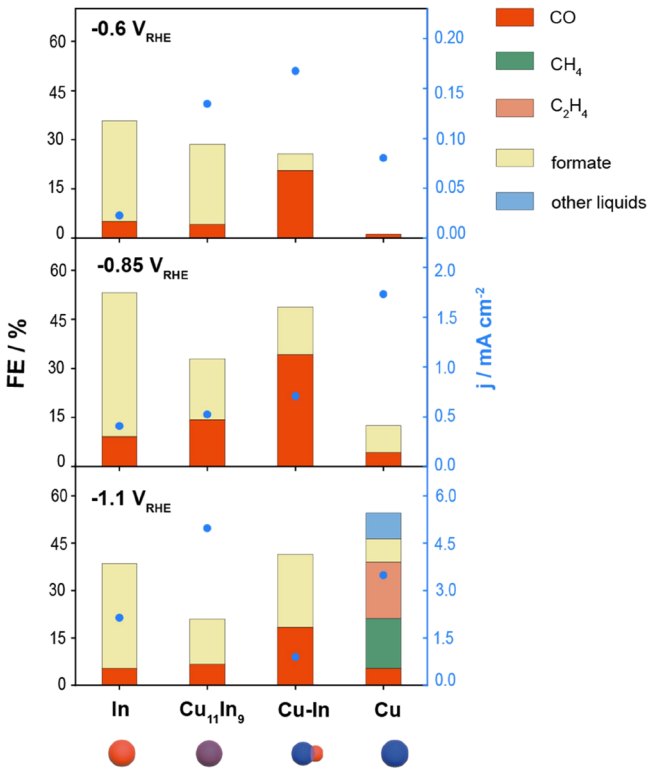

Figure 7. FEs of CO_2RR products (left axis) and geometric current densities, *j*, (right axis) of In, $Cu_{11}In_9$, dimer-like Cu-In, and Cu NCs. The remaining FE is provided by hydrogen and reported in Figure S14.

Cu-In dimers promote CO selectivity, with CO becoming the main CO_2RR product at the lower voltages, reaching a maximum FE_{CO} of around 35% and a formate/CO ratio of 0.4 at −0.85 V_{RHE} (Figure S12).

The measured products are consistent with those reported in the literature for Cu-In, which are CO, found as the main product in most studies, and formate, found with a similarly high selectivity in fewer studies.[35−43] However, the key features of the catalyst (i.e., morphology, elemental distribution, and interfaces) which determine which product evolves remain unclear.[35−43] This lack of clarity is related to the difficult comparison across the published studies where different preparation techniques result in Cu-In materials which are highly heterogeneous and differ in sizes and morphologies.[35−43] To understand the design rules which drive the selective formation of CO or formate is important as both chemicals are relevant for industry if produced in high yields and with more earth-abundant metals (Cu vs Ag or Au for CO and In for formate).[73] Our data collected on well-defined NCs, which all possess similar size and were all synthesized by the same approach, suggest that catalysts where In and Cu are homogeneously mixed have a tendency to produce formate, instead those where the two metals share an interface possess a higher selectivity for CO. We note that the Cu-In dimers possess a lower In content compared to the $Cu_{11}In_9$ (21% vs 40%); however, control experiments with physical mixtures of the two metals suggest that composition does not play a crucial role compared to interfaces (Figure S13). This novel insight will direct future studies toward the optimization of the electrode preparation (e.g., compositional tuning, loading, and deposition method) and device engineering (e.g., use of a

https://doi.org/10.1021/jacs.2c05792
J. Am. Chem. Soc. 2022, 144, 18286−18295

CO_2-fed electrochemical cell) to improve the overall performance of the Cu-In NC catalysts (i.e., current density and suppression of the hydrogen reduction reaction). Furthermore, operando studies to monitor the changes during CO_2RR are mandatory before we make any speculation on the mechanisms driving the selectivity.

CONCLUSIONS

In conclusion, we have explored the reactivity of colloidal In NCs in a GRR with a copper molecular precursor to synthesize Cu-In NCs with unprecedented monodispersity and tunability. Intermetallic, phase-segregated, and dimer-like NCs were obtained. All three bimetallic configurations were synthesized by tuning the reaction time and/or the amount of the added copper precursor, which both affect the extent of the galvanic exchange between copper ions and indium metal. We note that $Cu_{11}In_9$ NCs were synthesized before but with poor homogeneity.[74,75] The other In-Cu configurations are instead obtained for the first time. We demonstrated the utility of these newly synthesized structures as well-defined model catalysts to provide more insights into the Cu-In behavior in CO_2RR.

While proving that the GRR is a powerful approach to access diverse bimetallic structures, this work evidences that the common knowledge on GRR obtained via studies on noble metals, according to which alloyed nanoshells are expected to form, does not directly apply to oxophilic and poorly miscible metals. Importantly, we show how size-dependent kinetics and thermodynamics are crucial in understanding the outcome of GRR. We expect to inspire the bimetallic community into extending the GRRs to less explored and more oxophilic metal pairs.

ASSOCIATED CONTENT

Supporting Information

The Supporting Information is available free of charge at https://pubs.acs.org/doi/10.1021/jacs.2c05792.

Additional synthetic details, EM results and discussions, XRD Rietveld refinements, and Cu-In phase diagram (PDF)

AUTHOR INFORMATION

Corresponding Author

Raffaella Buonsanti − *Laboratory of Nanochemistry for Energy (LNCE), Institute of Chemical Sciences and Engineering, École Polytechnique Fédérale de Lausanne, Sion CH-1950, Switzerland;* orcid.org/0000-0002-6592-1869; Email: raffaella.buonsanti@epfl.ch

Authors

Laia Castilla-Amorós − *Laboratory of Nanochemistry for Energy (LNCE), Institute of Chemical Sciences and Engineering, École Polytechnique Fédérale de Lausanne, Sion CH-1950, Switzerland;* orcid.org/0000-0001-6212-0663

Pascal Schouwink − *Institute of Chemical Science and Engineering (ISIC), École Polytechnique Fédérale de Lausanne, Sion CH-1950, Switzerland*

Emad Oveisi − *Interdisciplinary Center for Electron Microscopy (CIME), École Polytechnique Fédérale de Lausanne, Lausanne CH-1015, Switzerland*

Valery Okatenko − *Laboratory of Nanochemistry for Energy (LNCE), Institute of Chemical Sciences and Engineering, École Polytechnique Fédérale de Lausanne, Sion CH-1950, Switzerland;* orcid.org/0000-0002-7542-7995

Complete contact information is available at: https://pubs.acs.org/10.1021/jacs.2c05792

Author Contributions

‖P.S. and E.O. equally contributed to this study.

Notes

The authors declare no competing financial interest.

ACKNOWLEDGMENTS

This work was primarily financed by the Swiss National Science Foundation (SNSF) under the grant no. 200021L_191997/1. The authors acknowledge Dr. Jan Vavra for initial microscopy characterization of one sample, Ludovic Zaza and Dr. Min Wang for the liquid chromatography measurements, and Dr. Alexander N. Chen and Dr. Anna Loiudice for helpful discussions.

REFERENCES

(1) Zhou, M.; Li, C.; Fang, J. Noble-Metal Based Random Alloy and Intermetallic Nanocrystals: Syntheses and Applications. *Chem. Rev.* **2021**, *121*, 736−795.

(2) Bu, L.; Shao, Q.; Pi, Y.; Yao, J.; Luo, M.; Lang, J.; Hwang, S.; Xin, H.; Huang, B.; Guo, J.; et al. Coupled S-p-d Exchange in Facet-Controlled Pd3Pb Tripods Enhances Oxygen Reduction Catalysis. *Chem* **2018**, *4*, 359−371.

(3) Wang, M.; Wang, L.; Li, H.; Du, W.; Khan, M. U.; Zhao, S.; Ma, C.; Li, Z.; Zeng, J. Ratio-Controlled Synthesis of CuNi Octahedra and Nanocubes with Enhanced Catalytic Activity. *J. Am. Chem. Soc.* **2015**, *137*, 14027−14030.

(4) Wang, S. B.; Zhu, W.; Ke, J.; Lin, M.; Zhang, Y. W. Pd-Rh Nanocrystals with Tunable Morphologies and Compositions as Efficient Catalysts toward Suzuki Cross-Coupling Reactions. *ACS Catal.* **2014**, *4*, 2298−2306.

(5) Cui, C.; Gan, L.; Li, H. H.; Yu, S. H.; Heggen, M.; Strasser, P. Octahedral PtNi Nanoparticle Catalysts: Exceptional Oxygen Reduction Activity by Tuning the Alloy Particle Surface Composition. *Nano Lett.* **2012**, *12*, 5885−5889.

(6) Huang, J.; Mensi, M.; Oveisi, E.; Mantella, V.; Buonsanti, R. Structural Sensitivities in Bimetallic Catalysts for Electrochemical CO 2 Reduction Revealed by Ag-Cu Nanodimers. *J. Am. Chem. Soc.* **2019**, *141*, 2490−2499.

(7) Gilroy, K. D.; Ruditskiy, A.; Peng, H. C.; Qin, D.; Xia, Y. Bimetallic Nanocrystals: Syntheses, Properties, and Applications. *Chem. Rev.* **2016**, *116*, 10414−10472.

(8) Liu, Y.; Hight Walker, A. R. Monodisperse Gold-Copper Bimetallic Nanocubes: Facile One-Step Synthesis with Controllable Size and Composition. *Angew. Chem., Int. Ed.* **2010**, *49*, 6781−6785.

(9) Xie, Y.; Cai, J.; Wu, Y.; Zang, Y.; Zheng, X.; Ye, J.; Cui, P.; Niu, S.; Liu, Y.; Zhu, J.; Liu, X.; Wang, G.; Qian, Y. Boosting Water Dissociation Kinetics on Pt−Ni Nanowires by N-Induced Orbital Tuning. *Adv. Mater.* **2019**, *31*, No. e1807780.

(10) Kim, D.; Resasco, J.; Yu, Y.; Asiri, A. M.; Yang, P. Synergistic Geometric and Electronic Effects for Electrochemical Reduction of Carbon Dioxide Using Gold-Copper Bimetallic Nanoparticles. *Nat. Commun.* **2014**, *5*, 4948.

(11) Goulas, K. A.; Sreekumar, S.; Song, Y.; Kharidehal, P.; Gunbas, G.; Dietrich, P. J.; Johnson, G. R.; Wang, Y. C.; Grippo, A. M.; Grabow, L. C.; et al. Synergistic Effects in Bimetallic Palladium-Copper Catalysts Improve Selectivity in Oxygenate Coupling Reactions. *J. Am. Chem. Soc.* **2016**, *138*, 6805−6812.

(12) Wang, Y.; Cao, L.; Libretto, N. J.; Li, X.; Li, C.; Wan, Y.; He, C.; Lee, J.; Gregg, J.; Zong, H.; Su, D.; Miller, J. T.; Mueller, T.; Wang, C. Ensemble Effect in Bimetallic Electrocatalysts for CO2 Reduction. *J. Am. Chem. Soc.* **2019**, *141*, 16635−16642.

(13) Ye, H.; Crooks, R. M. Effect of Elemental Composition of PtPd Bimetallic Nanoparticles Containing an Average of 180 Atoms on the Kinetics of the Electrochemical Oxygen Reduction Reaction. *J. Am. Chem. Soc.* **2007**, *129*, 3627−3633.
(14) Ren, X.; Lv, Q.; Liu, L.; Liu, B.; Wang, Y.; Liu, A.; Wu, G. Current Progress of Pt and Pt-Based Electrocatalysts Used for Fuel Cells. *Sustainable Energy Fuels* **2020**, *4*, 15−30.
(15) Peng, Y.; Cui, M.; Zhang, Z.; Shu, S.; Shi, X.; Brosnahan, J. T.; Liu, C.; Zhang, Y.; Godbold, P.; Zhang, X.; et al. Bimetallic Composition-Promoted Electrocatalytic Hydrodechlorination Reaction on Silver-Palladium Alloy Nanoparticles. *ACS Catal.* **2019**, 10803−10811.
(16) Kim, D.; Nam, H.; Cho, Y. H.; Yeo, B. C.; Cho, S. H.; Ahn, J. P.; Lee, K. Y.; Lee, S. Y.; Han, S. S. Unlocking the Potential of Nanoparticles Composed of Immiscible Elements for Direct H2O2 Synthesis. *ACS Catal.* **2019**, *9*, 8702−8711.
(17) Xie, C.; Chen, C.; Yu, Y.; Su, J.; Li, Y.; Somorjai, G. A.; Yang, P. Tandem Catalysis for CO2 Hydrogenation to C2-C4 Hydrocarbons. *Nano Lett.* **2017**, *17*, 3798−3802.
(18) Lin, M.; Kim, G. H.; Kim, J. H.; Oh, J. W.; Nam, J. M. Transformative Heterointerface Evolution and Plasmonic Tuning of Anisotropic Trimetallic Nanoparticles. *J. Am. Chem. Soc.* **2017**, *139*, 10180−10183.
(19) Yan, Y.; Du, J. S.; Gilroy, K. D.; Yang, D.; Xia, Y.; Zhang, H. Intermetallic Nanocrystals: Syntheses and Catalytic Applications. *Adv. Mater.* **2017**, *29*, No. 1605997.
(20) Yang, C.; Ko, B. H.; Hwang, S.; Liu, Z.; Yao, Y.; Luc, W.; Cui, M.; Malkani, A. S.; Li, T.; Wang, X.; et al. Overcoming Immiscibility toward Bimetallic Catalyst Library. *Sci. Adv.* **2020**, *6*, No. eaaz6844.
(21) Zhang, R. F.; Kong, X. F.; Wang, H. T.; Zhang, S. H.; Legut, D.; Sheng, S. H.; Srinivasan, S.; Rajan, K.; Germann, T. C. An Informatics Guided Classification of Miscible and Immiscible Binary Alloy Systems. *Sci. Rep.* **2017**, *7*, 9577.
(22) Osowiecki, W. T.; Ye, X.; Satish, P.; Bustillo, K. C.; Clark, E. L.; Alivisatos, A. P. Tailoring Morphology of Cu-Ag Nanocrescents and Core-Shell Nanocrystals Guided by a Thermodynamic Model. *J. Am. Chem. Soc.* **2018**, *140*, 8569−8577.
(23) Chen, P. C.; Gao, M.; Yu, S.; Jin, J.; Song, C.; Salmeron, M.; Scott, M. C.; Yang, P. Revealing the Phase Separation Behavior of Thermodynamically Immiscible Elements in a Nanoparticle. *Nano Lett.* **2021**, *21*, 6684−6689.
(24) Pohl, J.; Stahl, C.; Albe, K. Size-Dependent Phase Diagrams of Metallic Alloys: A Monte Carlo Simulation Study on Order-Disorder Transitions in Pt-Rh Nanoparticles. *Beilstein J. Nanotechnol.* **2012**, *3*, 1−11.
(25) Feng, J.; Chen, D.; Pikhitsa, P. V.; Jung, Y. H.; Yang, J.; Choi, M. Unconventional Alloys Confined in Nanoparticles: Building Blocks for New Matter. *Matter* **2020**, *3*, 1646−1663.
(26) He, M.; Protesescu, L.; Caputo, R.; Krumeich, F.; Kovalenko, M. V. A General Synthesis Strategy for Monodisperse Metallic and Metalloid Nanoparticles (In, Ga, Bi, Sb, Zn, Cu, Sn, and Their Alloys) via in Situ Formed Metal Long-Chain Amides. *Chem. Mater.* **2015**, *27*, 635−647.
(27) Castilla-Amorós, L.; Stoian, D.; Pankhurst, J. R.; Varandili, S. B.; Buonsanti, R. Exploring the Chemical Reactivity of Gallium Liquid Metal Nanoparticles in Galvanic Replacement. *J. Am. Chem. Soc.* **2020**, *142*, 19283−19290.
(28) Clarysse, J.; Moser, A.; Yarema, O.; Wood, V.; Yarema, M. Size- and Composition-Controlled Intermetallic Nanocrystals via Amalgamation Seeded Growth. *Sci. Adv.* **2021**, *7*, No. eabg1934.
(29) Kwon, S. G.; Krylova, G.; Phillips, P. J.; Klie, R. F.; Chattopadhyay, S.; Shibata, T.; Bunel, E. E.; Liu, Y.; Prakapenka, V. B.; Lee, B.; et al. Heterogeneous Nucleation and Shape Transformation of Multicomponent Metallic Nanostructures. *Nat. Mater.* **2015**, *14*, 215−223.
(30) Eikey, E. A.; Gan, X. Y.; Kaseman, D. C.; Murphey, C. G. E.; Crawford, S. E.; Johnston, K. A.; Yazdi, S.; Millstone, J. E. Efficient Control of Atom Arrangement in Ternary Metal Chalcogenide Nanoparticles Using Precursor Oxidation State. *Chem. Mater.* **2020**, *32*, 1322−1331.
(31) Hodges, J. M.; Morse, J. R.; Williams, M. E.; Schaak, R. E. Microscopic Investigation of Chemoselectivity in Ag-Pt-Fe3O4 Heterotrimer Formation: Mechanistic Insights and Implications for Controlling High-Order Hybrid Nanoparticle Morphology. *J. Am. Chem. Soc.* **2015**, *137*, 15493−15500.
(32) Mantella, V.; Castilla-Amorós, L.; Buonsanti, R. Shaping Non-Noble Metal Nanocrystals: Via Colloidal Chemistry. *Chem. Sci.* **2020**, *11*, 11394−11403.
(33) Asselin, J.; Boukouvala, C.; Wu, Y.; Hopper, E. R.; Collins, S. M.; Biggins, J. S.; Ringe, E. Decoration of Plasmonic Mg Nanoparticles by Partial Galvanic Replacement. *J. Chem. Phys.* **2019**, *151*, 244708.
(34) Okatenko, V.; Castilla-Amorós, L.; Stoian, D. C.; Vavra, J.; Loiudice, A. The Native Oxide Skin of Liquid Metal Ga Nanoparticles Prevents Their Rapid Coalescence during Electrocatalysis. *J. Am. Chem. Soc.* **2022**, *144*, 10053−10063.
(35) Rasul, S.; Anjum, D. H.; Jedidi, A.; Minenkov, Y.; Cavallo, L.; Takanabe, K. A Highly Selective Copper-Indium Bimetallic Electrocatalyst for the Electrochemical Reduction of Aqueous CO2 to CO. *Angew. Chem., Int. Ed.* **2015**, *54*, 2146−2150.
(36) Luo, W.; Xie, W.; Mutschler, R.; Oveisi, E.; De Gregorio, G. L.; Buonsanti, R.; Züttel, A. Selective and Stable Electroreduction of CO2 to CO at the Copper/Indium Interface. *ACS Catal.* **2018**, *8*, 6571−6581.
(37) Jang, Y. J.; Lee, J.; Kim, J. H.; Lee, B. J.; Lee, J. S. One-Dimensional CuIn Alloy Nanowires as a Robust and Efficient Electrocatalyst for Selective CO2-to-CO Conversion. *J. Power Sources* **2018**, *378*, 412−417.
(38) Wan, W.-B.; Dai, T.-Y.; Shi, H.; Zeng, S.-P.; Wen, Z.; Zhang, W.; Lang, X.-Y.; Jiang, Q. Intermetallic Cu11In9 in Situ Formed on Hierarchical Nanoporous Cu for Highly Selective CO2 Electroreduction. *J. Mater. Chem. A* **2022**, *10*, 4333−4343.
(39) Xiang, H.; Rasul, S.; Hou, B.; Portoles, J.; Cumpson, P.; Yu, E. H. Copper-Indium Binary Catalyst on a Gas Diffusion Electrode for High-Performance CO2 Electrochemical Reduction with Record CO Production Efficiency. *ACS Appl. Mater. Interfaces* **2020**, *12*, 601−608.
(40) Xie, Q.; Larrazábal, G. O.; Ma, M.; Chorkendorff, I.; Seger, B.; Luo, J. Copper-Indium Hydroxides Derived Electrocatalysts with Tunable Compositions for Electrochemical CO2 Reduction. *J. Energy Chem.* **2021**, *63*, 278−284.
(41) Larrazábal, G. O.; Shinagawa, T.; Martín, A. J.; Pérez-Ramírez, J. Microfabricated Electrodes Unravel the Role of Interfaces in Multicomponent Copper-Based CO2 Reduction Catalysts. *Nat. Commun.* **2018**, *9*, 1477.
(42) Larrazábal, G. O.; Martín, A. J.; Mitchell, S.; Hauert, R.; Pérez-Ramírez, J. Enhanced Reduction of CO2 to CO over Cu-In Electrocatalysts: Catalyst Evolution Is the Key. *ACS Catal.* **2016**, *6*, 6265−6274.
(43) Hoffman, Z. B.; Gray, T. S.; Moraveck, K. B.; Gunnoe, T. B.; Zangari, G. Electrochemical Reduction of Carbon Dioxide to Syngas and Formate at Dendritic Copper-Indium Electrocatalysts. *ACS Catal.* **2017**, *7*, 5381−5390.
(44) Shi, Z.; Tan, Q.; Tian, C.; Pan, Y.; Sun, X.; Zhang, J.; Wu, D. CO2 Hydrogenation to Methanol over Cu-In Intermetallic Catalysts: Effect of Reduction Temperature. *J. Catal.* **2019**, *379*, 78−89.
(45) Rahaman, M.; Andrei, V.; Pornrungroj, C.; Wright, D.; Baumberg, J. J.; Reisner, E. Selective CO Production from Aqueous CO2using a Cu96In4catalyst and Its Integration into a Bias-Free Solar Perovskite-BiVO4tandem Device. *Energy Environ. Sci.* **2020**, *13*, 3536−3543.
(46) Xia, X.; Wang, Y.; Ruditskiy, A.; Xia, Y. 25th Anniversary Article: Galvanic Replacement: A Simple and Versatile Route to Hollow Nanostructures with Tunable and Well-Controlled Properties. *Adv. Mater.* **2013**, *25*, 6313−6333.
(47) Sun, Y.; Mayers, B. T.; Xia, Y. Template-Engaged Replacement Reaction: A One-Step Approach to the Large-Scale Synthesis of Metal Nanostructures with Hollow Interiors. *Nano Lett.* **2002**, *2*, 481−485.

https://doi.org/10.1021/jacs.2c05792
J. Am. Chem. Soc. 2022, 144, 18286−18295

(48) Yang, Y.; Zhang, Q.; Fu, Z. W.; Qin, D. Transformation of Ag Nanocubes into Ag-Au Hollow Nanostructures with Enriched Ag Contents to Improve SERS Activity and Chemical Stability. *ACS Appl. Mater. Interfaces* **2014**, *6*, 3750−3757.
(49) Chen, A. N.; McClain, S. M.; House, S. D.; Yang, J. C.; Skrabalak, S. E. Mechanistic Study of Galvanic Replacement of Chemically Heterogeneous Templates. *Chem. Mater.* **2019**, *31*, 1344−1351.
(50) Oh, M. H.; Yu, T.; Yu, S.-H.; Lim, B.; Ko, K.-T.; Willinger, M.-G.; Seo, D.-H.; Kim, B. H.; Cho, M. G.; Park, J.-H.; et al. Galvanic Replacement Reactions in Metal Oxide Nanocrystals. *Science* **2013**, *340*, 964−968.
(51) Da Silva, A. G. M.; Rodrigues, T. S.; Haigh, S. J.; Camargo, P. H. C. Galvanic Replacement Reaction: Recent Developments for Engineering Metal Nanostructures towards Catalytic Applications. *Chem. Commun.* **2017**, *53*, 7135−7148.
(52) Hoshyargar, F.; Crawford, J.; O'Mullane, A. P. Galvanic Replacement of the Liquid Metal Galinstan. *J. Am. Chem. Soc.* **2017**, *139*, 1464−1471.
(53) Bahari, Z.; Dichi, E.; Legendre, B.; Dugué, J. The Equilibrium Phase Diagram of the Copper-Indium System: A New Investigation. *Thermochim. Acta* **2003**, *401*, 131−138.
(54) Nakagawa, T.; Mitsushima, S.; Okuyama, H.; Nishijima, M.; Aruga, T. Evolution of Geometric and Electronic Structure in Ultrathin In Films on Cu(001). *Phys. Rev. B* **2002**, *66*, No. 085402.
(55) Kermali, N. A.; Gabe, D. R. Diffusion Coating of Indium on Copper. *Surf. Technol.* **1982**, *15*, 1−10.
(56) Kim, D.-G.; Lee, C.-Y.; Jung, S. B. Interfacial Reactions and Intermetallic Compound Growth between Indium and Copper. *J. Mater. Sci.: Mater. Electron.* **2004**, *15*, 95−98.
(57) Buonsanti, R.; Grillo, V.; Carlino, E.; Giannini, C.; Kipp, T.; Cingolani, R.; Cozzoli, P. D. Nonhydrolytic Synthesis of High-Quality Anisotropically Shaped Brookite TiO2 Nanocrystals. *J. Am. Chem. Soc.* **2008**, *130*, 11223−11233.
(58) Ranade, M. R.; Navrotsky, A.; Zhang, H. Z.; Banfield, J. F.; Elder, S. H.; Zaban, A.; Borse, P. H.; Kulkarni, S. K.; Doran, G. S.; Whitfield, H. J. Energetics of Nanocrystalline TiO2. *Proc. Natl. Acad. Sci. U. S. A.* **2002**, *99*, 6476−6481.
(59) Li, X.; Chen, Q.; McCue, I.; Snyder, J.; Crozier, P.; Erlebacher, J.; Sieradzki, K. Dealloying of Noble-Metal Alloy Nanoparticles. *Nano Lett.* **2014**, *14*, 2569−2577.
(60) Liu, P.; Chen, Q.; Ito, Y.; Han, J.; Chu, S.; Wang, X.; Reddy, K. M.; Song, S.; Hirata, A.; Chen, M. Dealloying Kinetics of AgAu Nanoparticles by in Situ Liquid-Cell Scanning Transmission Electron Microscopy. *Nano Lett.* **2020**, *20*, 1944−1951.
(61) Cha, W.; Liu, Y.; You, H.; Stephenson, G. B.; Ulvestad, A. Dealloying in Individual Nanoparticles and Thin Film Grains: A Bragg Coherent Diffractive Imaging Study. *Adv. Funct. Mater.* **2017**, *27*, No. 1700331.
(62) Mondal, S.; Raj, C. R. Electrochemical Dealloying-Assisted Surface-Engineered Pd-Based Bifunctional Electrocatalyst for Formic Acid Oxidation and Oxygen Reduction. *ACS Appl. Mater. Interfaces* **2019**, *11*, 14110−14119.
(63) Oezaslan, M.; Heggen, M.; Strasser, P. Size-Dependent Morphology of Dealloyed Bimetallic Catalysts: Linking the Nano to the Macro Scale. *J. Am. Chem. Soc.* **2012**, *134*, 514−524.
(64) Anderson, B. D.; Tracy, J. B. Nanoparticle Conversion Chemistry: Kirkendall Effect, Galvanic Exchange, and Anion Exchange. *Nanoscale* **2014**, *6*, 12195−12216.
(65) Sun, Y.; Xia, Y. Alloying and Dealloying Processes Involved in the Preparation of Metal Nanoshells through a Galvanic Replacement Reaction. *Nano Lett.* **2003**, *3*, 1569−1572.
(66) Karvianto; Chow, G. M. Size-Dependent Transformation from Ag Templates to Au-Ag Nanoshells via Galvanic Replacement Reaction in Organic Medium. *J. Nanopart. Res.* **2012**, *14*, 1186.
(67) Ma, H.; Gao, P.; Qian, P.; Su, Y. Size-Dependent Electrochemical Properties of Pure Metallic Nanoparticles. *J. Phys. Chem. C* **2020**, *124*, 3403−3409.
(68) Shibata, T.; Bunker, B. A.; Zhang, Z.; Meisel, D.; Vardeman, C. F.; Gezelter, J. D. Size-Dependent Spontaneous Alloying of Au-Ag Nanoparticles. *J. Am. Chem. Soc.* **2002**, *124*, 11989−11996.
(69) Cojocaru, B.; Avram, D.; Kessler, V.; Parvulescu, V.; Seisenbaeva, G.; Tiseanu, C. Nanoscale Insights into Doping Behavior, Particle Size and Surface Effects in Trivalent Metal Doped. *Sci. Rep.* **2017**, *7*, 9598.
(70) Müller, C. J.; Lidin, S. Cu11In9 - Revised Crystal Structure and Its (Physicochemical) Relation to Cu10In7. *J. Alloys Compd.* **2015**, *638*, 393−397.
(71) Cunningham, P. D.; Coropceanu, I.; Mulloy, K.; Cho, W.; Talapin, D. V. Quantized Reaction Pathways for Solution Synthesis of Colloidal ZnSe Nanostructures: A Connection between Clusters, Nanowires, and Two-Dimensional Nanoplatelets. *ACS Nano* **2020**, *14*, 3847−3857.
(72) Liu, M.; Wang, R. Y. Size-Dependent Melting Behavior of Colloidal in, Sn, and Bi Nanocrystals. *Sci. Rep.* **2015**, *5*, 16353.
(73) Peplow, M. The Race to Recycle Carbon Dioxide. *Nature* **2022**, *603*, 780−783.
(74) Kind, C.; Feldmann, C.; Quintilla, A.; Ahlswede, E. Citrate-Capped Cu11In9 Nanoparticles and Its Use for Thin-Film Manufacturing of Cis Solar Cells. *Chem. Mater.* **2011**, *23*, 5269−5274.
(75) Lim, Y. S.; Jeong, J.; Kim, J. Y.; Ko, M. J.; Kim, H.; Kim, B.; Jeong, U.; Lee, D. K. Binder-Free Cu-in Alloy Nanoparticles Precursor and Their Phase Transformation to Chalcogenides for Solar Cell Applications. *J. Phys. Chem. C* **2013**, *117*, 11930−11940.

https://doi.org/10.1021/jacs.2c05792
J. Am. Chem. Soc. 2022, 144, 18286−18295